Ferroelastic Twin Angles at the Surface of $CaTiO_3$ Quantified by Photoemission Electron Microscopy

G. Magagnin,[1] C. Lubin,[1] M. Escher,[2] N. Weber,[2] L. Tortech,[3] and N. Barrett[1,*]
[1]SPEC, CEA, CNRS, Université Paris-Saclay, CEA Saclay, 91191 Gif-sur-Yvette, France
[2]Focus GmbH, Neukirchner Straße 2, D-65510 Hünstetten-Kesselbach, Germany
[3]NIMBE, CEA, CNRS, Université Paris-Saclay, CEA Saclay, 91191 Gif-sur-Yvette, France

(Received 24 May 2023; accepted 30 November 2023; published 29 January 2024)

We use photoemission electron microscopy to measure the ferroelastic twin wall angles at the surface of $CaTiO_3$ (001) and deduce the strain ordering. We analyze the angular dependence of the photoelectron emission from different domain surfaces, each with its own characteristic tilt angle in the factory rooflike topography. By considering the surface topography as a field perturbation, the offset in the photoemission threshold can be directly related to the tilt angles. With knowledge of the symmetry allowed twin walls we quantify the twin angles between 179.1° to 180.8°.

DOI: 10.1103/PhysRevLett.132.056201

At twin boundaries in ferroelastic materials, the spontaneous strain changes sign over only a few nanometers [1] giving rise to strong gradients which can generate new properties quite distinct from those of the adjacent domains. Superconductivity [2], polarity [3,4], and chirality [4] have all been reported in twin walls. Such emerging functionalities are absent in the bulk [5,6] and provide a new perspective of "the material is the machine" [7]. In addition, their nanometric dimensions make them potentially 2D functional objects.

The polar character of twin walls was predicted theoretically [8] and simulations suggest that twin wall polarity in $CaTiO_3$ and $SrTiO_3$ [9] can be switched by an applied field [10]. If this were the case then ferroelastic materials with ferroelectric twin walls would be promising for robust, high-density information storage. Harnessing such functionality requires controlling wall polarity at the surface which, in turn, depends on the strain state of the adjacent domains.

Twinning gives rise to surface topography with a characteristic factory rooflike structure. Each twin has a distinct angle at the surface, often within a degree of 180° (flat surface), defined by the strain tensor compatibility across the wall [11]. The tensors in turn define the local strain gradients and therefore directly influence both the magnitude of the wall polarity and, potentially, the switching field. Novak and Salje studied the distribution of lattice strain near the intersection of surface layers and twin boundaries [12]. They found that twin boundaries close to the surface are expected to generate local polarization via the flexoelectric [13] (or other) coupling effects [14]. Quantification of the twin angles at the surface of ferroelastic materials is therefore an essential step in understanding the electromechanical coupling between strain and polarity.

$CaTiO_3$ is the archetypal perovskite, ferroelastic below 1150° C with a *Pbnm* orthorhombic structure. It consists of corner-linked TiO_6 octahedra with Ca atoms sitting in between, distorted from the ideal cubic perovskite by two independent octahedral tilts, written as $a^-a^-c^+$ in Glazer notation [15]. By symmetry, one of the tilts goes to zero at the twin wall, allowing for the emergence of a competing secondary order parameter [4]. Biquadratic coupling between the primary and secondary order parameter yields two equivalent ground states for the wall polarity [14]. However, the flexoelectric induced strong polarization [16] may break inversion symmetry and favor a specific polarization direction in the twin wall.

Twin walls in $CaTiO_3$ have been studied using aberration-corrected transmission electron microscopy [3]. Second harmonic generation provides another proof of the loss of inversion symmetry [11] but with a spatial resolution limited to 0.5 μm. Eliseev *et al.* have carried out a theoretical study of the DW/surface intersection in $CaTiO_3$ [17]. However, few direct measurements of the twin angles have been made. Electron imaging of charged (ferroelectric) surfaces was proposed by Le Bihan [18] and successfully applied to visualize ferroelastic domains in barium titanate while low energy electron microscopy has yielded valuable data on $CaTiO_3$ surface topography and structure [19,20].

Energy-filtered photoemission electron microscopy (PEEM) is a nondestructive, surface-sensitive imaging technique with a high spatial and energy resolution. Contrast in PEEM arises from local chemistry, work function [21], electrical topography, or physical topography [22,23]. We have developed a quantitative approach using the specificities of photoemission electron microscopy to determine the twin angle present at the surface of $CaTiO_3$ thanks to a simple model of the imaging electron optics.

In PEEM, electrons cross the diffraction plane on the optical axis for normal emission and off axis for off-normal emission. By positioning an aperture in the back focal plane, a given angular range can be selected to quantify the twin angles.

Optical microscopy is also sensitive to the surface topography, however, the lateral resolution of PEEM (∼50 nm) is much better than optical microscopy. The most widespread technique for measuring surface topography is atomic force microscopy although tip-surface contact can be an issue for AFM and furthermore it is a scanning technique. The parallel imaging in PEEM allows acquisition of topography over a full field of view. The methodology presented here would be very attractive, for example, for measuring the microscopic topography on either side of a ferroelastic phase transition. Moreover, the topography quantification in PEEM can be combined with x-ray linear dichroism imaging in XAS-PEEM [24] to extract information on orbital ordering.

The sample is a $CaTiO_3$ (001) single crystal from SurfaceNet GmbH. Before introduction into the vacuum system, the sample was exposed for 5 min to ozone at room temperature to remove the organic contamination. Annealing at 650°C in vacuum is used to desorb the oxidized contaminants and produces near surface oxygen vacancies, helping to alleviate charging problems during the photoemission process [19]. Experiments were carried out at 300°C to further avoid charging. A focused He I source (21.2 eV) was used in a ScientaOmicron Nano-ESCA II PEEM. Photoemission threshold image series are acquired as a function of the electron energy with respect to the sample holder Fermi level, $E - E_F$, in steps of 50 meV and with an energy resolution of 100 meV, as determined by the analyzer slit and pass energy. Images are normalized with respect to the signal from a homogeneous area of the sample in order to account for detector inhomogeneities. The image series were analyzed using an automatic procedure fitting the pixel-by-pixel threshold spectra with an error function [25]. The nonisochromaticity in the vertical direction due to the dispersion in the hemispherical imaging analyzer is corrected [25]. The contrast aperture (CA) in the back focal plane has a diameter of 150 μm. Image series were acquired for CA positions between −230 μm and +230 μm in steps of 10 μm with respect to the optical axis.

Complementary AFM was performed using a Nano-Observer (CS-Instruments) in contact mode with FORTA tips (AppNano) with stiffness of 1.6 N/m to characterize the surface without scratching.

The effect of the CA is shown in the schematic of Fig. 1(b). Higher off-centering of the CA improves dramatically the domain topography contrast in PEEM thanks to the angular selection but also induces a shift of the energy scale. Off-normal electrons have velocity components perpendicular and parallel to the sample surface; as a result, the kinetic energy measured inside the PEEM will be slightly lower, and the threshold for photoemission is shifted to higher energy within the reference frame of the PEEM.

Emission from domains with different tilt angles are centered at different positions in the diffraction plane, giving rise to intensity variation as shown in Figs. 1(d)–1(f) via the angular selection by the CA [Fig. 1(b)]. We focus on the domains labeled D_1, D_2, $D_{1'}$, and D_3. Domain D_1 is used for PEEM electron optics alignment and the surface normal coincides with the PEEM optical axis. D_2, D_3, and $D_{1'}$ have finite tilt angles with respect to D_1. The twin wall is vertical in the image, therefore, by

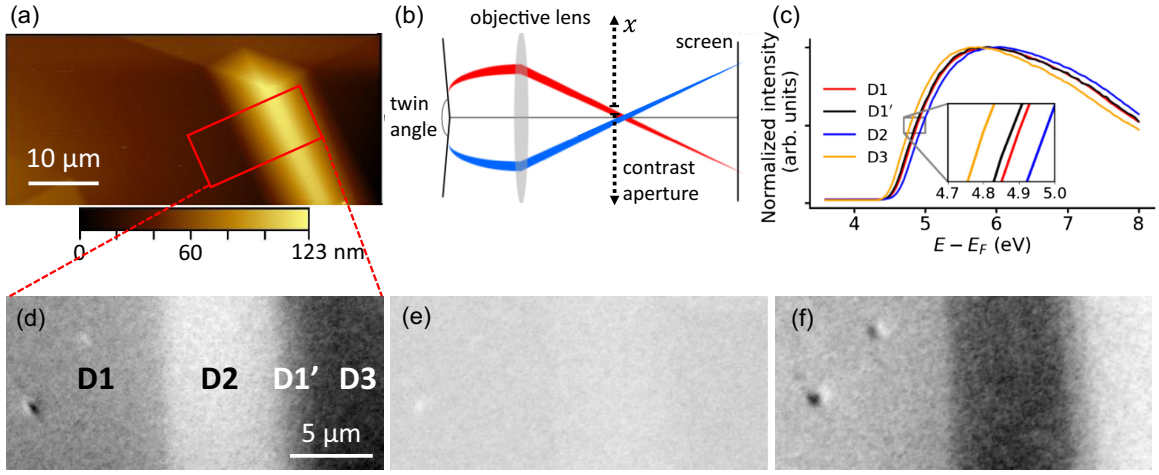

FIG. 1. (a) AFM topography image of the $CaTiO_3$ surface with a red box highlighting the area of interest containing domains D_1, D_2, $D_{1'}$ and D_3. The surface topography is visible with the twin D_2/D_3 on the right hand side. (b) Schematic showing the angular selection by the contrast aperture in the back focal plane of photoelectron emission from twin domains, here the electron emission in red is favored. (c) Photoemission threshold spectra from domains D_1, D_2, and D_3 (d)–(f) PEEM images acquired at $E - E_f = 4.3$ eV for CA positions +140, 0, and −140 μm with respect to the optical axis.

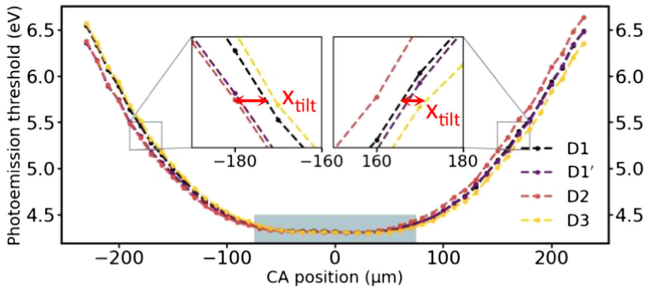

FIG. 2. Photoemission threshold in domains D_1 to D_3 with the contrast aperture off-centered from −230 μm to +230 μm. The insets show the rigid threshold energy shift depending on the surface ferroelastic domains D_1 to D_3. The gray shaded area represents the 150 μm CA.

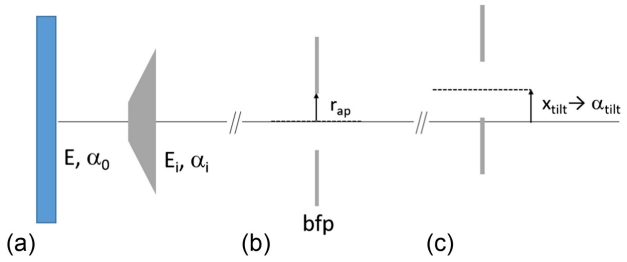

FIG. 3. (a) Electrons are emitted with energy E and at an angle α in the laboratory reference frame are transported at E_i in the PEEM making an angle α_i with the optical axis. (b) CA of radius r_{ap} centered in the objective lens back focal plane. (c) CA off-centered at x_{tilt} corresponding to the angular deviation in the PEEM due to α_{tilt} of the domain twin.

off-centering the CA horizontally we selectively analyze photoelectrons emitted from domains [Figs. 1(d) and 1(f)] on either side of a twin boundary. When the CA is centered on the optical axis, the contrast between the twin domains is almost zero. In this configuration, the angular difference with respect to D_1 is minimized as in Fig. 1(e). Figure 1(c) shows the spectra for each domain extracted from the threshold image series.

The threshold values over the domains are obtained by performing a pixel-by-pixel fit to the spectra with an error function, giving a map of threshold values, as detailed in Supplemental Material [26]. Figure 2 shows the evolution of the photoemission threshold for D_1, D_2, $D_{1'}$, and D_3 of Fig. 1 as a function of the CA position from −230 μm to +230 μm.

Close to the optical axis, the measured threshold is constant at 4.05 eV. When the CA is off-centered further than its physical radius (~75 μm), electrons on the optical axis are physically blocked, effectively switching to a dark field imaging mode where higher angle emission from one side of the optical axis is enhanced at the expense of emission from the other side. The contrast between domains is enhanced [Figs. 1(d) and 1(f)] not only because the threshold value increases but also because the difference between domain thresholds, as measured by PEEM, increases. The threshold energy curves have the same form but they are not centered at the same CA position. D_2 and D_3 have surface tilts of opposite signs and are rigidly shifted, respectively, to the left and right with respect to that of D_1 and $D_{1'}$. When the domain surface is tilted by an angle α_{tilt} the photoelectron intensity in the back focal plane is also off-centered by a distance x_{tilt}, experimentally obtained from the centroid of the two parabolic branches in Fig. 2. Therefore, by measuring the shift in the threshold curves and with a knowledge of the electron optics, it should be possible to quantify the twin angles, as suggested in Fig. 3.

Phase conservation in the PEEM is given by

$$\sqrt{E} r_0 \sin(\alpha_0) = \sqrt{E_i} r_i \sin(\alpha_i) \tag{1}$$

where α_0 the emission angle with respect to the sample normal, E the emitted electron energy, E_i the electron energy in the PEEM column, α_i the electron angle with respect to the optical axis in the PEEM. The objective lens magnification M is defined as r_i/r_0. For small angles, $\sin(\alpha_i) = (x/l)$ where l is the distance between the CA and the first image plane. For simplicity, we assume an isotropic electron emission up to 90°, i.e., $\alpha = 90°$. For a tilted surface, the optical axis in the back focal plane is shifted by x_{tilt}. The photoemission threshold E_{thr} is given by Eq. (2) (details in Supplemental Material [26]).

$$E_{thr} = \frac{E_i M}{l^2}(x + x_{tilt} \pm r_{ap})^2. \tag{2}$$

The evolution of the photoemission threshold with the CA lateral position is therefore a stretched parabola with a flat central range defined by r_{ap} of constant minimum threshold. In the NanoESCA setup, $l = 165$ mm, $M = 32$, and $E_i = 2000$ eV, which allows us to extract x_{tilt} at each pixel. From x_{tilt}, we can then work back to the surface tilt angle α_{tilt} by considering a periodic triangular surface topography as a perturbation of the local electric field [27] (details in Supplemental Material [26]). Equation (3) expresses the relation between the surface tilt angle α_{tilt} and the CA position in the back focal plane x_{tilt}.

$$\alpha_{tilt} = c_k \frac{\pi^2}{4} \left(\frac{\sqrt{2 m_e e U_o}}{\hbar} \sqrt{\frac{L}{d}} \right)^{-1} x_{tilt}, \tag{3}$$

with c_k is the conversion factor between position in the back focal plane and reciprocal lattice vector for the PEEM settings used here (4.14 $Å^{-1}\,m\,m^{-1}$), m_e the electron mass, U_0 the bias between the sample and extractor (20 kV), $2L = 20$ μm as a typical value for the periodicity in surface topography and $d = 2.5$ mm the distance between the sample and extractor. The angle map is represented in Fig. 4(a) and compared with that measured by AFM.

There is a good qualitative agreement between the PEEM and AFM maps. The PEEM analysis correctly

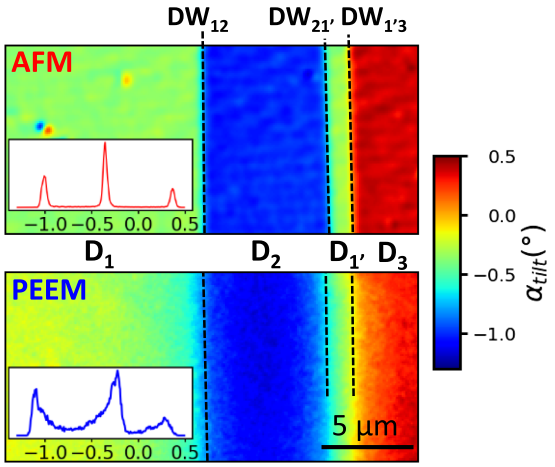

FIG. 4. PEEM and AFM angular maps of the analyzed area, with an indication of the domain walls. Insets with the histogram of the angles extracted from the AFM and PEEM maps and correspondence with D_1 to D_3.

discriminates the ferroelastic domains D_1, D_2, $D_{1'}$, and D_3. Surfaces tilted with a positive or negative angle are revealed and the narrow domain $D_{1'}$ between D_2 and D_3, which has the same angle as D_1 is also resolved. The latter has a domain width of ∼1.7 μm. It should be noted that the usual method in the PEEM of imaging in the reciprocal space to deduce surface angles would have been impossible for a domain this small since it is beyond the limit of usual field apertures. High resolution real-space imaging to deduce angular maps with the submicron resolution is necessary.

The histograms of the PEEM and AFM angular maps are shown in the insets of Fig. 4. The overall angular range, as determined by PEEM is between −1.25° and 0.45°, in agreement with the known $CaTiO_3$ twin angles [19]. D_2 and D_3, centered at −1.0° and +0.4°, respectively, show good agreement between AFM and PEEM. The main discrepancy between the two angular maps remains the tilt angle of D_1. This is due to the residual alignment offset between PEEM and AFM.

The angular spread for D_1 and D_2 is much smaller in AFM compared to the PEEM, typically 0.05° compared to 0.15°. The approximation of the perturbation in Supplemental Material [26] was done for the middle of the terraces. At the edges one could expect an additional angular divergence since the electrons may be more strongly influenced by the neighbouring domain structures on their way to the extractor. The higher angular spread for the PEEM data may also be related to the angular dependence in the y direction due to the 24° azimuthal sample rotation in the PEEM frame. For the narrower domains, D_2 and D_3, higher order terms in the triangular perturbation are likely to have a non-negligible effect on the angular spread. Finally, the PEEM acquires data by parallel imaging at fixed lens parameters. There is a weak correlation even for microscopic fields of view between position and take-off angle which adds to the angular broadening

TABLE I. Domain wall twin angles and their corresponding spontaneous strain pairs. The uncertainty corresponds to 2σ.

	DW_{12}	$DW_{21'}$	$DW_{1'3}$
Twin angle	$179.1° \pm 0.2°$	$180.7 \pm 0.2°$	$180.8 \pm 0.2°$
Strain state	S_{vi}/S_{iii}	S_{iii}/S_{iv}	S_{iv}/S_{v}

whereas AFM acquires data sequentially, at each data point measuring the same slope, and is immune to angular crosstalk.

The twin angles calculated from the α_{tilt} values are $DW_{12} = 179.1° \pm 0.2°$, $DW_{21'} = 180.7 \pm 0.2°$, and $DW_{1'3} = 180.8 \pm 0.2°$ and are reported in Table I.

There are six possible spontaneous strain orientations in $CaTiO_3$ which satisfy stain compatibility deduced from symmetry [11,19,28]. Given the experimental angles, the twin walls are of type W [11] and are described by $x = \pm y$. From the sequence 179.1°/180.9°/180.9°, we deduce a strain ordering of $S_{vi}/S_{iii}/S_{iv}/S_{v}$ (Supplemental Material [26]), as represented in Fig. 5 and summarized in Table I.

This analysis is limited to domains aligned vertically in the PEEM, i.e., running orthogonal to the lateral displacement of the CA. It would be straightforward to extend the methodology to two dimensions to analyze twin structures along all combinations of ⟨100⟩ and ⟨110⟩ by using the full x-y in-plane positions of the CA. As discussed, the finite CA radius gives rise to an angular spread, however, in the limit of small angles, this does not influence the mean twin angle. The angular range is given by the small α_{tilt} approximation $\tan^{-1}(H/L) \approx (H/L)$ and the uncertainty is better than 0.1° (Fig. S4).

The measurement of the surface topography by PEEM can be easily extended to other materials showing surface elastic ordering. The methodology could be used to characterize materials showing surface topography coupling with a functional property (electrical polarization, magnetism). For example, the shear strain induced magnetoelectric coupling between a ferroelectric and a

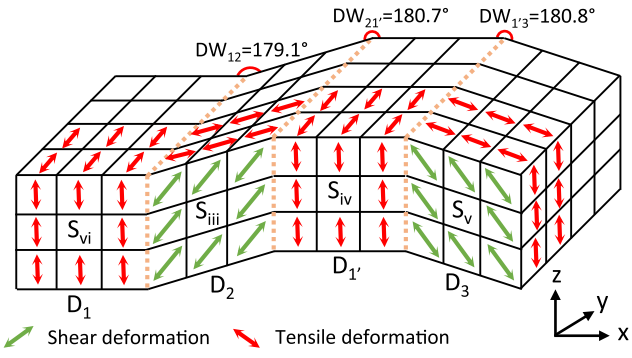

FIG. 5. Schematic of the spontaneous strain configuration in the analyzed area with its indexed spontaneous domain strains, reported in Supplemental Material [26].

magnetic thin film [29] could be quantified for individual ferroelectric domains, opening the way to the development of strain-mediated nanoscale devices. The martensitic transition in CuZnAl and thin-film NiTiCu shape memory alloys, shows work function contrast between martensite plates [30] and should give rise to surface tilt angles due to the plate formation. Magnetic Heusler shape-memory alloys are also dependent on the magnetic field direction arising from a specific surface topography [31]. Tilt angle quantification through the martensitic phase transition by PEEM could identify the magnetization directions and enable correlation with magnetocaloric properties. A more directly technological application could be the spatially resolved characterization of Si wafer bowing as a function of processing conditions, which can be a key factor in device reliability [32].

We have used threshold PEEM imaging to measure twin angles at the surface of ferroelastic $CaTiO_3$ with its characteristic factory rooflike structure. By off-centering the contrast aperture from the optical axis, contrast due to the physical surface topography is enhanced by collecting high angular photoelectrons in a near dark-field mode. Electrons emitted at higher angles have a higher apparent value of the photoemission threshold. Using a model of the electron optics, integrating the perturbation of the extractor field by surface twin topography we can quantify the twin angles, and by comparison with the symmetry allowed twin walls we can deduce directly the surface strain ordering. The results agree well with the independent measurements by AFM. They provide a unique insight into electromechanical coupling responsible for twin wall polarity at the surface and, potentially, a handle to control twin wall polarity.

*nick.barrett@cea.fr

[1] S. A. Hayward, J. Chrosch, E. K. H. Salje, and M. A. Carpenter, Eur. J. Mineral. **8**, 1301 (1997).

[2] A. Aird and E. K. H. Salje, J. Phys. Condens. Matter **10**, L377 (1998).

[3] S. Van Aert, S. Turner, R. Delville, D. Schryvers, G. Van Tendeloo, and E. K. H. Salje, Adv. Mater. **24**, 523 (2012).

[4] L. Goncalves-Ferreira, S. A. Redfern, E. Artacho, and E. K. Salje, Phys. Rev. Lett. **101**, 097602 (2008).

[5] E. Salje and H. Zhang, Phase Transitions **82**, 452 (2009).

[6] D. D. Viehland and E. K. Salje, Adv. Phys. **63**, 267 (2014).

[7] K. Bhattacharya and R. D. James, Science **307**, 53 (2005).

[8] V. Janovec and J. Přívratská, in *International Tables for Crystallography* (International Union of Crystallography, Chester, England, 2006), pp. 449–505.

[9] J. F. Scott, E. K. Salje, and M. A. Carpenter, Phys. Rev. Lett. **109**, 187601 (2012).

[10] T. Zykova-Timan and E. K. Salje, Appl. Phys. Lett. **104**, 082907 (2014).

[11] H. Yokota, H. Usami, R. Haumont, P. Hicher, J. Kaneshiro, E. K. Salje, and Y. Uesu, Phys. Rev. B **89**, 144109 (2014).

[12] J. Novak and E. K. H. Salje, J. Phys. Condens. Matter **10**, L359 (1998).

[13] P. Zubko, G. Catalan, and A. K. Tagantsev, Annu. Rev. Mater. Res. **43**, 387 (2013).

[14] E. K. H. Salje, S. Li, M. Stengel, P. Gumbsch, and X. Ding, Phys. Rev. B **94**, 024114 (2016).

[15] A. M. Glazer, Acta Crystallogr. Sect. B **28**, 3384 (1972).

[16] M. Stengel, Phys. Rev. B **88**, 174106 (2013).

[17] E. A. Eliseev, A. N. Morozovska, Y. Gu, A. Y. Borisevich, L. Q. Chen, V. Gopalan, and S. V. Kalinin, Phys. Rev. B **86**, 085416 (2012).

[18] R. Le Bihan, Ferroelectrics **97**, 19 (1989).

[19] G. F. Nataf, M. Guennou, J. Kreisel, P. Hicher, R. Haumont, O. Aktas, E. K. H. Salje, L. Tortech, C. Mathieu, D. Martinotti, and N. Barrett, Phys. Rev. Mater. **1**, 074410 (2017).

[20] Z. Zhao, N. Barrett, Q. Wu, D. Martinotti, L. Tortech, R. Haumont, M. Pellen, and E. K. H. Salje, Phys. Rev. Mater. **3**, 043601 (2019).

[21] M. Escher, K. Winkler, O. Renault, and N. Barrett, J. Electron Spectrosc. Relat. Phenom. **178–179**, 303 (2010).

[22] S. A. Nepijko, N. N. Sedov, C. Ziethen, G. Schonhense, M. Merkel, and M. Escher, J. Microsc. **199**, 124 (2000).

[23] M. Lavayssière, M. Escher, O. Renault, D. Mariolle, and N. Barrett, J. Electron Spectrosc. Relat. Phenom. **186**, 30 (2013).

[24] E. Arenholz, G. Van Der Laan, A. Fraile-Rodríguez, P. Yu, Q. He, and R. Ramesh, Phys. Rev. B **82**, 140103(R) (2010).

[25] N. Barrett, J. E. Rault, J. L. Wang, C. Mathieu, A. Locatelli, T. O. Mentes, M. A. Niño, S. Fusil, M. Bibes, A. Barthélémy, D. Sando, W. Ren, S. Prosandeev, L. Bellaiche, B. Vilquin, A. Petraru, I. P. Krug, and C. M. Schneider, J. Appl. Phys. **113**, 187217 (2013).

[26] See Supplemental Material at http://link.aps.org/supplemental/10.1103/PhysRevLett.132.056201 for the electron optics model of the perturbation of the extractor field by the surface twin topography.

[27] A. Bok, A mirror electron microscope, Ph.D. thesis, 1968, http://resolver.tudelft.nl/uuid:a0046b97-8e35-4878-bb4c-ebc065727e20.

[28] J. Sapriel, Phys. Rev. B **12**, 5128 (1975).

[29] M. Ghidini, R. Mansell, F. Maccherozzi, X. Moya, L. C. Phillips, W. Yan, D. Pesquera, C. H. W. Barnes, R. P. Cowburn, J.-M. Hu, S. S. Dhesi, and N. D. Mathur, Nat. Mater. **18**, 840 (2019).

[30] M. Cai, S. Langford, J. Dickinson, G. Xiong, T. Droubay, A. Joly, K. Beck, and W. Hess, J. Nucl. Mater. **361**, 306 (2007).

[31] A. Planes, L. Mañosa, and M. Acet, J. Phys. Condens. Matter **21**, 233201 (2009).

[32] T. Islam, J. Zechner, M. Bernardoni, M. Nelhiebel, and R. Pippan, Rev. Sci. Instrum. **88**, 024709 (2017).